

# Excitons in nonlinear optical responses: shift current in MoS<sub>2</sub> and GeS monolayers

J.J. Esteve-Paredes,<sup>1,\*</sup> M. A. García-Blázquez,<sup>1</sup> A. J. Uría-Álvarez,<sup>1</sup> M. Camarasa-Gómez,<sup>2</sup> and J.J. Palacios<sup>1,3,4</sup>

<sup>1</sup>*Departamento de Física de la Materia Condensada,  
Universidad Autónoma de Madrid, E-28049 Madrid, Spain*

<sup>2</sup>*Department of Molecular Chemistry and Materials Science,  
Weizmann Institute of Science, Rehovot 7610001, Israel*

<sup>3</sup>*Instituto Nicolás Cabrera (INC), Universidad Autónoma de Madrid, E-28049 Madrid, Spain.*

<sup>4</sup>*Condensed Matter Physics Center (IFIMAC), Universidad Autónoma de Madrid, E-28049 Madrid, Spain.*

(Dated: June 21, 2024)

It is well-known that exciton effects are determinant to understand the optical absorption spectrum of low-dimensional materials. However, the role of excitons in nonlinear optical responses has been much less investigated at an experimental level. Additionally, computational methods to calculate nonlinear conductivities in real materials are still not widespread, particularly taking into account excitonic interactions. We present a methodology to calculate the excitonic second-order optical responses in 2D materials relying on: (i) *ab initio* tight-binding Hamiltonians obtained by Wannier interpolation and (ii) the Bethe-Salpeter equation with effective electron-hole interactions. Here, in particular, we explore the role of excitons in the shift current of monolayer materials. Focusing on MoS<sub>2</sub> and GeS monolayer systems, our results show that *2p*-like excitons, which are dark in the linear response regime, yield a contribution to the photocurrent comparable to that of *1s*-like excitons. Under radiation with intensity  $\sim 10^4$  W/cm<sup>2</sup>, the excitonic theory predicts in-gap photogalvanic currents of almost  $\sim 10$  nA in sufficiently clean samples, which is typically one order of magnitude higher than the value predicted by independent-particle theory near the band edge.

## I. INTRODUCTION

Excitons are key to our understanding of the linear optical response in low-dimensional semiconductors and insulators. Examples can be found in nanotubes [1, 2] and quasi-two-dimensional (2D) crystals [3, 4]. In these systems, the combined effect of quantum confinement and a weak screening environment lead to large excitonic binding energies [5–7]. This fact manifests in strong peaks below the quasi-particle gap in photoluminescence and optical absorption experiments. From the theory point of view, the linear response formalism plus the Bethe-Salpeter equation (BSE) for exciton calculations have been proven to be powerful tools to explain the measured optical responses in the low-field regime [8–14].

In the nonlinear regime, the bulk photovoltaic or photogalvanic effect [15] (abbreviated BPVE or PGE) is a nonlinear effect of second order that has attracted much interest lately (see Ref. [16] for a review). It refers to the generation of a direct current (DC) in the bulk of a non-centrosymmetric material under light radiance, and thus it has an inherent potential for application in solar-cell devices. The BPVE was early explored in ferroelectric materials [17, 18], and continued gathering attention during the next decades [19–23] until nowadays, as experiments achieve a high-efficiency in power conversion [24]. More recently, low-dimensional materials are also being explored in this regard. For instance, it has been shown that a large BPVE occurs in WS<sub>2</sub> nanotubes [25, 26] and nanoribbons [27], strained 3R-MoS<sub>2</sub> and phosphorene [28, 29], monolayer MoSe<sub>2</sub> [30], SnS [31, 32], or one-dimensional grain boundaries [33].

The characterization and rationalization of the experimental signatures of the BPVE is a current active field of

research [34, 35]. On the theoretical side, methods based on the independent-particle approximation (IPA) for the band structure and Bloch eigenstates are widely used to calculate the second order and frequency-dependent conductivities [36–46]. This level of theory is sometimes successful, specially in bulk materials [34, 37, 47, 48], while in other experiments the measured values of the photogalvanic currents are nearly one order of magnitude different than the predicted ones [25, 26], or show features that indicate the need for a many-body description of the problem [35]. It is therefore necessary to develop a more complete theory of the nonlinear optical response that goes beyond a purely IPA description, in order to achieve a reliable characterization of the BPVE in real materials. As shown below, including electron-hole interactions makes a huge difference.

In the literature, electron-hole interaction effects have been addressed in two scenarios. First, in the study of the so-called *ballistic* current [16], which originates from asymmetric carrier generation in the Brillouin zone (BZ) and is considered to be an incoherent process (with its own relaxation time). Here, electron-hole interactions seem to have a minor effect both in bulk and 2D systems [49]. On the other hand, more recent works have considered the effect of excitons within the coherent nonlinear optical response formalism [50, 51]. Additionally, the role of excitons in 2D materials has been investigated by Green's function methods in the time domain [52, 53]. These few works show that excitons are equally or even more dominant in the non-linear response of low-dimensional materials than in the linear response.

In this work, we present a methodology to compute the second-order optical conductivity which takes into account electron-hole interactions, updating previous ap-

proaches to linear optical properties based on tight-binding methods [9–11, 54–56]. Here we start from an ab initio tight-binding description of the band structure, obtained by Wannier interpolation. Importantly, the use of a Wannier Hamiltonian ensures that all relevant dipole matrix elements in the local basis are properly accounted for, which gives a description of optical responses more accurately than a purely effective tight-binding approximation [57–59]. Secondly, electron hole interactions are included by solving the BSE with effectively-screened electron-hole interactions. As a proof of concept, we focus on the evaluation of the shift current, which, in the absence of magnetism and under radiation with linearly-polarized light. This current-response is clearly discernible in experiments and understood with theoretical calculations [17, 18, 34, 35, 37, 48].

As case examples, we study  $2H$ -MoS<sub>2</sub> and GeS monolayers. The former is a prototypical TMDC material, showing a rich structure of exciton levels due to the important role played by spin-orbit coupling (SOC), while the latter is often taken as a test case for its simplicity and possibly very large shift current [38, 39, 52, 58]. We compute the shift current as a function of the frequency of the incident radiation, as it would be measured in a photocurrent spectroscopy experiment [25, 30]. We show that excitonic effects red-shift the IPA frequency-dependent response function, generally increasing the shift current by nearly an order of magnitude. This happens by the appearance of a finite and sometimes dominant contribution at energies below the band gap. Interestingly, we also show that  $2p$ -like excitons, dark in linear response, are *bright* in the second-order optical response and, therefore, can give a contribution to the BPVE.

Our work is organized as follows. In Sec. II we review the theoretical framework to calculate exciton states and to evaluate the second-rank conductivity tensor corresponding to the shift current. In Sec. III we show our numerical results of the different frequency-dependent quantities, both with and without electron-hole interactions. Finally, in IV we summarize our conclusions and future-work perspectives.

## II. METHODS

### A. Quasi-particle band structure and excitons

From a many-body perspective, the study of the exciton physics in a gapped material requires first the evaluation of its quasi-particle band structure. To carry out this task, one typically introduces electron-electron interactions beyond the Kohn-Sham density functional theory (DFT) level by calculating a self-energy correction to the bands,  $\varepsilon_n(\mathbf{k}) = \varepsilon_n^{\text{KS}}(\mathbf{k}) + \Sigma_n(\mathbf{k})$ . The self-energy is typically obtained within the GW approximation [8], where dynamical and local-field effects are included. Alternatively, hybrid-functionals can be used to obtain a satisfactory quasi-particle band structure (for instance, the

band gaps are larger than those obtained from standard DFT) at possibly lower computational cost than that of GW methods.

Within this scenario, we will assume that a Wannier interpolation [60, 61] to the best-available quasi-particle band structure has been carried out. We also assume that a set of well-localized  $n_{\text{orb}}$  Wannier orbitals, which we denote  $w_\alpha(\mathbf{r} - \mathbf{d}_\alpha - \mathbf{R}) = \langle \mathbf{r} | \alpha \mathbf{R} \rangle$ , has been found. Bloch states built with these functions,  $|\alpha \mathbf{k}\rangle = 1/\sqrt{N} \sum_{\mathbf{R}} e^{i\mathbf{k}\cdot\mathbf{R}} |\alpha \mathbf{R}\rangle$ , are referred to as Bloch-Wannier states. The single-particle Hamiltonian projected on these states is given by

$$H_{\alpha\alpha'}^{(\text{W})}(\mathbf{k}) = \sum_{\mathbf{R}} e^{i\mathbf{k}\cdot\mathbf{R}} \langle \alpha \mathbf{0} | \hat{H} | \alpha' \mathbf{R} \rangle. \quad (1)$$

Note from the phase factor in (1) we choose the so-called *lattice* gauge, whereas the *atomic* gauge is another convention that is present in the literature [62, 63] [64]. Diagonalization of the  $n_{\text{orb}} \times n_{\text{orb}}$  Hamiltonian matrix yields the Wannier-interpolated energy eigenvalues,

$$[U^\dagger(\mathbf{k})H^{(\text{W})}(\mathbf{k})U(\mathbf{k})]_{nn'} = \varepsilon_n(\mathbf{k})\delta_{nn'}, \quad (2)$$

where  $U(\mathbf{k})$  is the unitary transformation matrix containing the Bloch eigenstates coefficients  $c_{n\alpha}(\mathbf{k})$  in the expansion of the band-structure eigenstates  $|n\mathbf{k}\rangle = \sum_{\alpha} c_{n\alpha}(\mathbf{k}) |\alpha \mathbf{k}\rangle$ .

Excitons arise from the Coulomb interaction of a quasi-electron and quasi-hole, some of them forming bound states within the bandgap. Using valence ( $v$ ) and conduction ( $c$ ) single-particle states, we expand exciton states of zero center of mass momentum ( $\mathbf{Q} = 0$ ) in a basis of free electron-hole pairs as  $|X_N\rangle = \sum_{v\mathbf{c}\mathbf{k}} A_{v\mathbf{c}\mathbf{k}}^{(N)}(\mathbf{k}) \hat{c}_{\mathbf{c}\mathbf{k}}^\dagger \hat{c}_{v\mathbf{k}} |0\rangle$ , being  $|0\rangle$  the ground state, identified as the Fermi sea. Exciton states are thus found by solving the BSE [65] in the Tamm-Dancoff approximation

$$(\varepsilon_{c\mathbf{k}} - \varepsilon_{v\mathbf{k}})A_{v\mathbf{c}}^{(N)}(\mathbf{k}) + \sum_{v'\mathbf{c}'\mathbf{k}'} \langle v\mathbf{c}\mathbf{k} | K_{\text{eh}} | v'\mathbf{c}'\mathbf{k}' \rangle A_{v'\mathbf{c}'}(\mathbf{k}') = E_N A_{v\mathbf{c}}(\mathbf{k}), \quad (3)$$

where  $K_{\text{eh}} = -(D - X)$  is the electron-hole interaction kernel, including the direct ( $D$ ) and exchange terms ( $X$ ). The direct term reads

$$D_{v\mathbf{c},v'\mathbf{c}'}(\mathbf{k}, \mathbf{k}') = \int \psi_{c\mathbf{k}}^*(\mathbf{r}) \psi_{v'\mathbf{k}'}^*(\mathbf{r}') W(\mathbf{r}, \mathbf{r}') \psi_{c'\mathbf{k}'}(\mathbf{r}) \psi_{v\mathbf{k}}(\mathbf{r}'), \quad (4)$$

and we treat the screened Coulomb interaction  $W$  in the static limit. The exchange term in the kernel is obtained by interchanging  $c'\mathbf{k}'$  and  $v\mathbf{k}$ . Fully ab initio calculations, namely GW-BSE methods, often employ an unscreened exchange interaction, as derived using many-body perturbation theory (MBPT) techniques [65]. Recent studies point out the necessity of constructing an effective screening for the exchange in some scenarios [66], such as core-conduction excitations. In our variational approach where the BSE can be seen as the result of representing the Hamiltonian in a Hilbert space expanded by

one-electron excitations Slater determinants, it is natural to assume the same screening for all Coulomb matrix elements [11, 67].

In this work, we model the 2D screening environment by using a Rytova-Keldysh potential [68]. In the case of vacuum surroundings, this model has one parameter, the screening length  $r_0$ , which can actually be calculated from DFT [68]. The choice of the 2D interaction model may be determinant for the resulting exciton energy series and the envelope wave functions (recent computational packages [56, 69] allow to explore other different potentials). In the case of layered materials of much interest such as heterostructures or one-dimensional systems, other interaction models have also been proposed [70, 71] and can be considered for future studies.

The Wannier orbitals  $w_\alpha(\mathbf{r} - \mathbf{d}_\alpha - \mathbf{R}) = \langle \mathbf{r} | \alpha \mathbf{R} \rangle$  have a finite spread that may be of the order of several unit cells. To efficiently implement Eq. (4), here we ignore the real-space details of the orbitals, treating them as delta-like functions peaked at their centers [10, 54, 56, 69]. The actual shape of the orbitals has been taken into consideration by other authors [67], although we skip this numerical refinement in exchange for less computational and technical burden. The computational efficiency of this approach depends significantly on whether Coulomb integrals are performed in real or reciprocal space. We use a real-space implementation [54], which allows to cast the Coulomb interaction matrix elements in a bilinear form that is amenable for vectorizing calculations [56]. Below, we show that our results for the exciton structure in monolayer MoS<sub>2</sub> are in agreement with previous literature, which is a successful test for our methodology.

## B. Nonlinear optical response

In a general manner, the frequency-dependent second-order current-density reads

$$j_a^{(2)}(\omega) = \int d\omega_p \int d\omega_q \sum_{bc} \sigma_{abc}^{(2)}(\omega; \omega_p, \omega_q) \times \varepsilon_b(\omega_p) \varepsilon_c(\omega_q) \delta([\omega_p + \omega_q] - \omega) \quad (5)$$

The contribution to the BPVE can be extracted by taking the DC limit. Here, we focus on the response under radiation with linearly-polarized light, known as shift current (in the absence of magnetic effects). The amount and directionality of the DC shift-current response depends on the frequency of the incident pulse, which can be expressed in terms of the second-order conductivity tensor at zero frequency [36, 72, 73]:

$$j_a^{(2, \text{sh})} = 2 \sum_{bc} \text{Re}[\sigma_{abc}^{(\text{sh})}(0, \omega, -\omega) \varepsilon_b(\omega) \varepsilon_c(-\omega)], \quad (6)$$

where we have considered radiation under monochromatic light. The shift conductivity tensor (or simply shift conductivity) can be derived either in the velocity

or length light-matter interaction gauges. Only the latter choice ensures the fastest convergence rates as well as the most accurate spectra for any basis size, and is also free from low-frequency divergences (see Ref. [74] and references therein). In the IPA, the shift conductivity tensor reads

$$\sigma_{abc}^{(\text{sh})}(0, \omega, -\omega) = -\frac{i\pi e^3}{2\hbar V} \sum_{nn'\mathbf{k}} f_{nn'\mathbf{k}} [I_{nn'\mathbf{k}}^{abc} + I_{nn'\mathbf{k}}^{acb}] \times \delta(\omega - \omega_{nn'\mathbf{k}}), \quad (7)$$

where the strength of the transitions is  $I_{nn'\mathbf{k}}^{abc} = r_{nn'\mathbf{k}}^b r_{n'n\mathbf{k}}^{c;a}$ , and the matrix elements are

$$r_{nn'\mathbf{k}}^a = (1 - \delta_{nn'}) \xi_{nn'\mathbf{k}}^a, \quad (8)$$

$$r_{nn'\mathbf{k}}^{a;b} = \nabla_b r_{nn'\mathbf{k}}^a - i r_{nn'\mathbf{k}}^a [\xi_{nn\mathbf{k}}^b - \xi_{n'n'\mathbf{k}}^b],$$

being  $\xi_{nn'\mathbf{k}}^a$  the Berry connection and  $r_{nn'\mathbf{k}}^{a;b}$  the generalized derivative of  $r_{nn'\mathbf{k}}^a$ . While the off-diagonal Berry connections can be related to matrix elements of velocity operator, the generalized derivative presents the issue of computing the diagonal elements  $\xi_{nn\mathbf{k}}^a$ , which suffer from phase indetermination in numerical approaches. To circumvent this problem, an alternative approach is the use of sum rules [74] to directly evaluate  $r_{nn'\mathbf{k}}^{a;b}$ , now only involving velocity matrix elements between remote energy bands. In a Wannier-interpolation scheme, these remote bands may be out of the wannierized subspace and therefore not available to be included in calculations. While this problem can still be mitigated by means of perturbation theory [58], here we set a numerical algorithm to smooth the phase of eigenvectors (see our previous work [73] and the *Supplementary Material*). As a result,  $\mathbf{k}$ -derivatives of matrix elements can be evaluated numerically and the generalized derivative can be computed *exactly*.

In a similar fashion, a version of Eq. (7) including exciton effects can be written [75, 76], but now involving matrix elements between excitonic many-body states. We extract the shift conductivity by taking the real part of the second order conductivity tensor at zero frequency [76]

$$\sigma_{abc}^{(\text{sh})}(0; \omega, -\omega) = \frac{e^3}{\hbar V} \sum_{NN'} \text{Re}(S_{NN'}^{abc}) \times [\delta(\hbar\omega - E_N) + \delta(\hbar\omega + E_N)]. \quad (9)$$

where we have defined the exciton coupling matrix element  $S_{NN'}^{abc} \equiv i R_{0N}^a R_{NN'}^b R_{N'0}^c$ , being  $R_{0N}^a = \langle \text{GS} | \hat{r}_a | X_N \rangle$  and  $R_{NN'}^a = \langle X_N | \hat{r}_a | X_{N'} \rangle$  with GS denoting the ground state. Further details about excitonic matrix elements are given in the *Supplementary Material*. The same phase criteria is applied to single-particle eigenvectors when constructing the BSE matrix in Eq. (3) (note that it

depends on the single-particle eigenvectors via the direct and exchange terms), which allows to agree on the phase choice between  $A_{vc\mathbf{k}}^{(N)}$  and single-particle matrix elements, ensuring that exciton matrix elements are properly evaluated.

### C. Post-processing workflow

We have developed a post-processing workflow to evaluate Eqs. (7) and (9). After the evaluation of the DFT band structure, the WANNIER90 [61] code is used to obtain a maximally-localized Wannier interpolation of the quasi-particle band structure. The Hamiltonian and dipole matrix elements between Wannier orbitals are printed, which is sufficient to evaluate the linear and non-linear responses in the IPA. To include exciton effects, the output of WANNIER90 is interfaced with XATU [56], which yields the exciton energies and wavefunctions as output. Eq. (9) is finally implemented using the previous building blocks.

## III. NUMERICAL RESULTS

### A. 1L-MoS<sub>2</sub>

#### 1. Band structure and computational details

We start by calculating the quasiparticle band structure of monolayer MoS<sub>2</sub>, as shown in Fig. 1(a). In the single-particle calculations, a SRSB functional [77, 78] has been employed, yielding a direct gap of 2.60 eV at the *K* point. We include spin-orbit coupling (SOC) in the calculation, yielding a top valence band splitting of 0.17 eV. These values are in good agreement with previous calculations (see e.g. [12, 13]). In a post-processing step, we obtain a Wannier Hamiltonian [60, 61] for the manifold of the 16 highest valence bands and 8 bottom conduction bands.

Next, we include exciton effects by solving the BSE. We use our recently developed package XATU to solve Eq. (3), as explained previously. To extract our results, we perform calculations using a dimension of  $N_k^2 \times n_v \times n_c = 102^2 \times 2 \times 2$  in the Hilbert space when solving the BSE. For further analysis, we name the energy bands as  $(v_{-1}, v_0, c_1, c_2)$  in order of increasing energy at the *K* point. We consider a screening length of  $r_0 = 35$  Å and vacuum surroundings in the Rytova-Keldysh potential, similarly to previous studies [79]. For a fair comparison between the non-interacting and excitonic results, below we restrict to the same subspace of bands when evaluating the optical responses in the IPA.

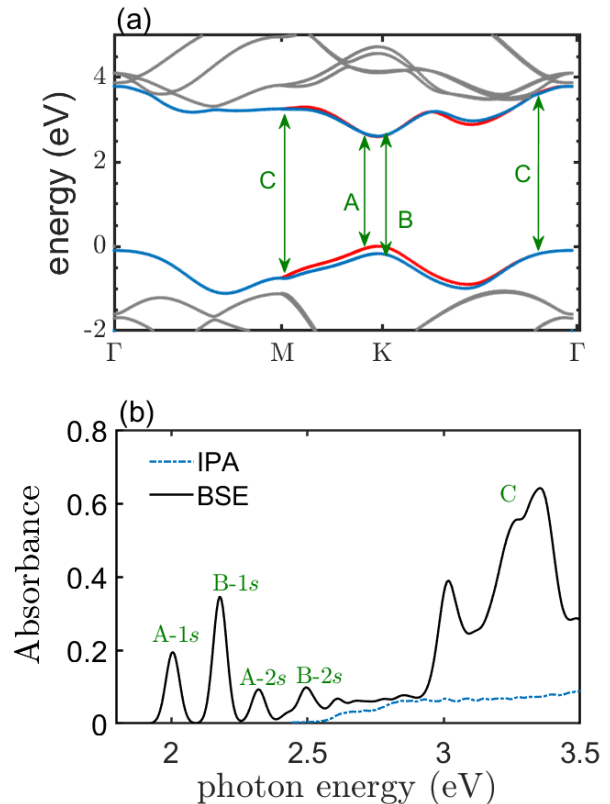


FIG. 1. (a) Band structure of monolayer MoS<sub>2</sub> including SOC. Blue (red) bands have its eigenstates formed by mostly spin-up (spin-down) Bloch-Wannier states. We have pointed the position of the most relevant electron-hole excitation to the wavefunction of the labeled excitons in the absorbance spectrum. Bands that are not included in the BSE calculation are in grey color. (b) Absorbance of monolayer MoS<sub>2</sub> as calculated in the independent-particle approximation and including exciton effects.

#### 2. Exciton spectrum

We briefly review here the characteristics of the excitons in MoS<sub>2</sub> based on the output of our methodology. To understand the exciton spectrum, special attention needs to be paid to the spin structure of the BSE. Since  $S_z$  is a good quantum number in the vicinity of the *K* and *K'* points, the interacting BSE Hamiltonian almost decouples into a set of solutions with like or unlike spin of electron-hole pairs. Only excitons formed by spin-conserving electron-hole pairs are expected to have enough oscillator strength to be bright. SOC-induced band-splitting gives rise to two series of excitons. Around the *K* point, the lowest-energy electron-hole pair excitation with the same spin is  $(v_0, c_1)$ . Accordingly, equal-energy electron-hole excitations occur at *K'* with inverted spin character, due to time reversal symmetry. Excitons that are mainly formed by these electron-hole free pairs constitute the A series. The next like-spin free electron-hole excitations,  $(v_{-1}, c_2)$  gives a different series

of excitons, called B.

Within the A series, we find the following structure for the exciton shell structure:  $1s$  at 2.00 eV,  $2p$  at 2.26 eV,  $2s$  at 2.32 eV,  $3d$  at 2.37 eV, and  $3s$  at 2.43 eV. A similar B series is found blueshifted (in overall) by 0.17 eV, which is the  $A$ - $B$  split of the  $1s$  exciton. The angular momenta character is assigned by inspecting the node structure of  $A_{vc}^{(N)}(\mathbf{k})$ . Our numerical results show that the lowest-energy exciton of the spectrum is formed by unlike-spin transitions around  $K$  and  $K'$  valleys, red-shifted from the optically bright A- $1s$  exciton by 25 meV. The previous spin structure of levels and our numerical results are in very good agreement with ab initio, tight-binding and model calculations [7, 10–12, 54, 80], which tests our methodology and allow us to step into the study of optical responses.

### 3. Light absorbance

We start exploring the optical responses by examining the frequency-dependent absorbance of monolayer MoS<sub>2</sub>, which is based on the evaluation of the linear conductivity (see the *Supplementary Material*). For the current analysis, we have calculated the frequency-dependent spectrum both in the IPA approximation and after including excitons. We set a broadening  $\eta = 25$  meV throughout the rest of the work.

In Fig. 1(b) we show the frequency-dependent absorbance of light under linearly polarized light. The IPA curve displays a typical step-like shape up to our range of inspection, as more bands come into play in the  $M-K-\Gamma$  path. When interactions are considered, the bright excitons become visible below the quasi-particle band gap. As discussed, SOC induces two series of excitons which are clearly identified. Higher in energy, we identify the noticeable C resonance around 3 eV, which corresponds to the excitons formed by electron-hole pairs in the continuum. Previous studies have shown that more bands are needed in order to fully resolve the magnitude of the C resonance [10], hence we do not analyze it here any further. Apart from bright  $s$ -type excitons, the  $p$ -like ones can also be optically active in  $D_{3h}$  monolayers [55, 81]. However, due to the small trigonal warping effect in MoS<sub>2</sub> around the  $K$  point, the latter have a vanishing oscillator strength [82] and are not visible in absorbance or transmittance spectra, in agreement with our numerical calculations.

### 4. Shift conductivity

We now turn into the main set of results in this work, in regards to the nonlinear optical response. We start by evaluating the frequency-dependent shift conductivity tensor entries, as explained in the theory section. If the  $x$  axis is along the armchair direction, and taking into account the  $D_{3h}$  symmetry of monolayer TMDCs, one can

check that  $\sigma_{xxx} = -\sigma_{xyy} = -\sigma_{xyx} = -\sigma_{xxy}$  while the other components are null [73]. Note that the symmetry arguments to determine the shape of the tensor are the same as in the single-particle picture, since they can be made from Eq. (6). We therefore restrict our analysis to  $\sigma_{xxx}$ . Below, we present results neglecting the exchange interaction in the BSE, which is a common assumption in the literature when using effective models. Actually, the inclusion of the exchange interaction noticeably changes the results, as shown in the *Supplementary Material*, although our discussion is equally valid with and without exchange effects.

In Fig. 2, we show  $\sigma_{xxx}^{(sh)}(0; \omega, -\omega)$  for monolayer MoS<sub>2</sub>, as computed in the IPA using Eq. (7) and including exciton effects using Eq. (9). The IPA shift conductivity is positive and barely varying in the shown energy range. Interactions red-shift features that can be found in the IPA calculations at larger energies (see *Supplementary Material* for the complete IPA curve), bringing them into the selected energy window, while adding new ones. First, we identify the in-gap exciton resonances and label its angular momentum character. We observe that the A- $1s$  and B- $1s$  resonances have a response of  $\sim 8$  nm  $\cdot$   $\mu A/V^2$ , which is roughly 3 times bigger than the IPA response near the band-gap. Differently from the linear absorbance case, we observe peaks corresponding to  $p$  excitons. This feature can be understood by comparing the expressions of the linear and nonlinear oscillator strengths, and the magnitude of dipole matrix elements between exciton states. In MoS<sub>2</sub>, the low trigonal warping around the  $K$  points yields that  $|R_{0,2p}| \simeq 0.05|R_{0,1s}|$ , and as the linear oscillator strength is  $\sim |R_{0N}|^2$ , the brightness of  $p$  excitons is strongly suppressed with respect to  $s$  excitons. In contrast, the nonlinear oscillator strength behaves as  $S_{NN'} \sim R_{0N}R_{NN'}R_{N'0}$  (normalized to the total volume). The similar value of the conductivity for the  $1s$  and  $2p$  excitons is understood by inspecting their coupling matrix elements. Our results yield that  $|R_{1s,1s}|$  and  $|R_{2s,2p}|$  are particularly small, so inter-exciton couplings are responsible for the finite shift conductivity at those resonances. Our numerical results show that  $|R_{1s,2p}| \sim 10|R_{0,1s}| \sim 200|R_{0,2p}|$ . The small value of  $R_{0,2p}$  in the triple product of matrix elements is counteracted by a strong inter-exciton coupling and allows the  $p$  exciton to be visible in the shift conductivity spectrum with a similar brightness than the  $1s$  exciton. This selection rules have been treated previously in the second harmonic generation optical response [83], and also by recent ab initio calculations [84].

Above the quasi-particle gap, we observe the C resonance whose shape is similar to the non-interacting case. Previous results based on tight-binding excitons [10] have shown that adding more bands to the calculation can enlarge the optical response of this part of the spectrum up to 25 %. Calculations with larger Hilbert spaces, needed to converge this part of the spectrum, are postponed for future work.

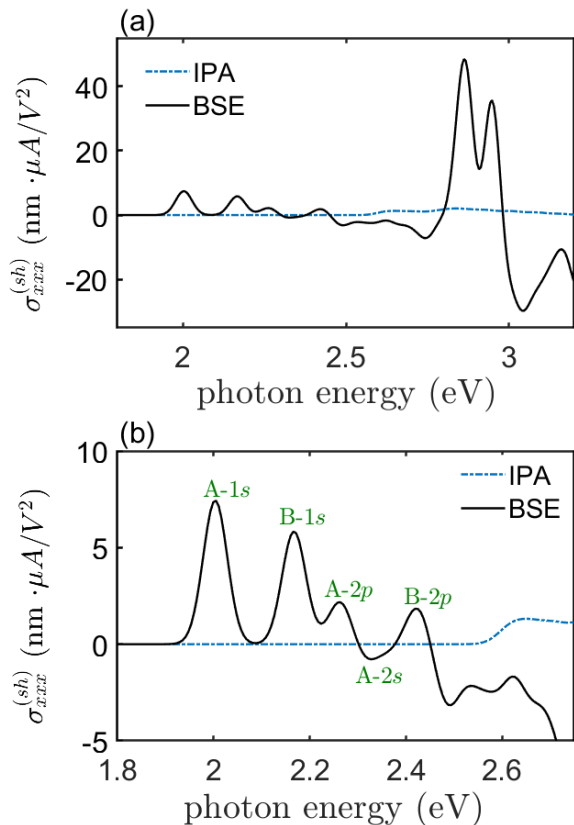


FIG. 2. (a) Frequency-dependent shift conductivity of monolayer MoS<sub>2</sub> calculated in the IPA approximation and including exciton effects. See main text for discussion. (b) In-gap excitonic shift conductivity, as zoomed in from (a). Resonances are labeled according to the exciton spectrum.

## B. 1L-GeS

### 1. Band structure and exciton spectrum

We now revisit the case of monolayer GeS, whose shift current response in presence of exciton effects has been investigated by an ab initio time-dependent scheme [52]. Our analysis below adds extra insightful information about the relevant excitons giving rise to a large shift conductivity.

In Fig. 3(a) we show the band structure of monolayer GeS calculated using a SRSF functional. SOC is not included as it is expected to be small. Our calculations yield a direct gap at  $\Gamma$  of 2.72 eV. In a post-processing step, we obtain a Wannier Hamiltonian [60, 61] for the manifold of the top 20 valence bands and first 7 conduction bands. Next, we include exciton effects by solving the BSE using the same dimension than in the previous example. In this case, we set a screening length to  $r_0 = 20 \text{ \AA}$  [85].

According to Fig. 3(a), the lowest-energy and direct electron-hole excitation across the bandgap occurs at  $\Gamma$ , followed by an excitation along the  $\Gamma$ -X path, which we

denote with  $V_x$  following a previous study [85]. As a consequence, our calculations show that the first five bound exciton states are formed by a linear combination of  $e$ - $h$  pairs around  $\Gamma$ , while the fifth in energy is formed in the  $V_x$  region. We label them according to its angular momentum character:  $\Gamma$ -1s at 1.82 eV,  $\Gamma$ -2p<sub>1</sub> at 2.11 eV,  $\Gamma$ -2p<sub>2</sub> at 2.21 eV,  $\Gamma$ -3p at 2.26 eV, and  $V_x$ -1s at 2.36 eV. We elaborate in the following on the optical response of such excitons in the optical response.

### 2. Light absorbance and shift conductivity

Fig. 3(b) shows the optical absorbance with and without exciton effects, using light polarized along the armchair (aligned with the  $x$  axis) and zigzag directions of monolayer GeS. The case of armchair polarization shows two big peaks that are assigned to the  $\Gamma$ -1s and  $V_x$ -1s excitons. Remarkably, the  $\Gamma$ -3p exciton is also considerably bright, which denotes the departure from the isotropic and hydrogen-like model for excitons. The zigzag case, shown in Fig 3(c), shows an almost dark in-gap spectrum. We identify the first peak with the  $\Gamma$ -2p<sub>1</sub>, whose oscillator strength is appreciable in this case. The  $\Gamma$ -2p<sub>2</sub> level is thus the only exciton that is dark in absorbance.

Due the  $C_{2v}$  point group of monolayer GeS, in this case with the  $c_2$  rotation axis along the  $x$  (in-plane) direction, the non-vanishing in-plane components of the shift conductivity are  $\sigma_{xxx}$ ,  $\sigma_{xyy}$ ,  $\sigma_{yyx} = \sigma_{yxy}$  [73]. We focus our analysis in  $\sigma_{xxx}$  and  $\sigma_{xyy}$ , which are shown in Fig 4(a) and (b). The  $\sigma_{xxx}^{(sh)}$  component shows that its main in-gap contribution comes from 1s-like excitons, with opposite directionality. This fact can be understood by considering the non-interacting limit for the shift conductivity: the  $\Gamma$  and  $V_x$  regions in the BZ give a contribution of different sign to the shift conductivity, which can be seen in the IPA curve around 3 eV. Thus, exciton formed in such regions inherit this feature. By inspecting excitonic matrix elements, we conclude that the  $\Gamma$ -1s exciton has main contributions from the intra-exciton  $S_{\Gamma-1s,\Gamma-1s}$  and inter-exciton  $S_{\Gamma-2p_2,\Gamma-1s}$ . The former matrix element is two orders of magnitude than the equivalent in MoS<sub>2</sub>. We attribute this difference to a larger effective mass occurring in monolayer GeS at  $\Gamma$  plus the large anisotropy effect, which depart excitons in GeS from the hydrogen-like picture in the electron hole interaction.

As in MoS<sub>2</sub>, the  $\Gamma$ -p<sub>2</sub> becomes bright in the shift conductivity spectrum. Our numerical results show that half of its response comes from the coupling  $S_{\Gamma-1s,\Gamma-2p_2}$  while the other half comes from the coupling with excitons at higher energies. Finally, we check that the  $V_x$ -1s exciton response arise mainly from its intra-exciton coupling matrix elements. As shown in the *Supplementary Material*, its wavefunction does not overlap with excitons formed around  $\Gamma$ , therefore the coupling with exciton at lower energies is vanishing. On the other hand,  $\sigma_{xyy}^{(sh)}$  shows little low-energy response, as no bright excitons can be coupled through the nonlinear oscillator strength. At

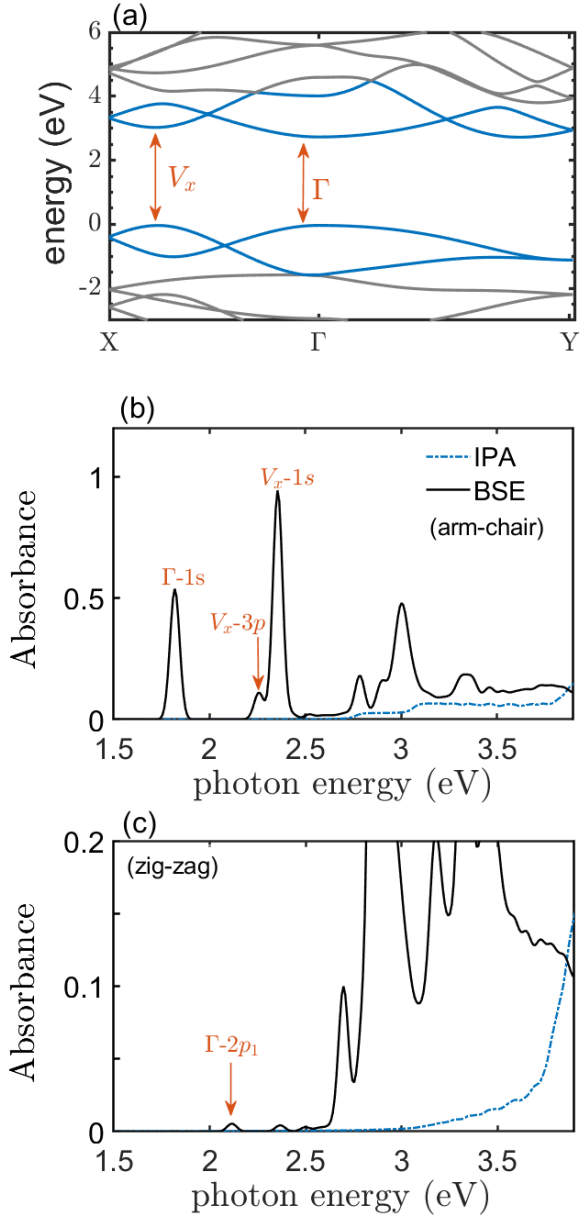


FIG. 3. (a) Band structure of monolayer GeS (SOC has been not included). Arrows mark the position of the most relevant electron-hole excitation to the wavefunction of the labeled excitons in the absorbance spectrum. Bands that are not included in the BSE calculation are in grey color. (b) Absorbance of monolayer GeS as calculated in the IPA approximation and including exciton effects for light polarized in the arm-chair direction. (c) Same as (b) but for zig-zag polarization.

higher energies, this tensor components reaches similar minimum values as the  $xxx$  component.

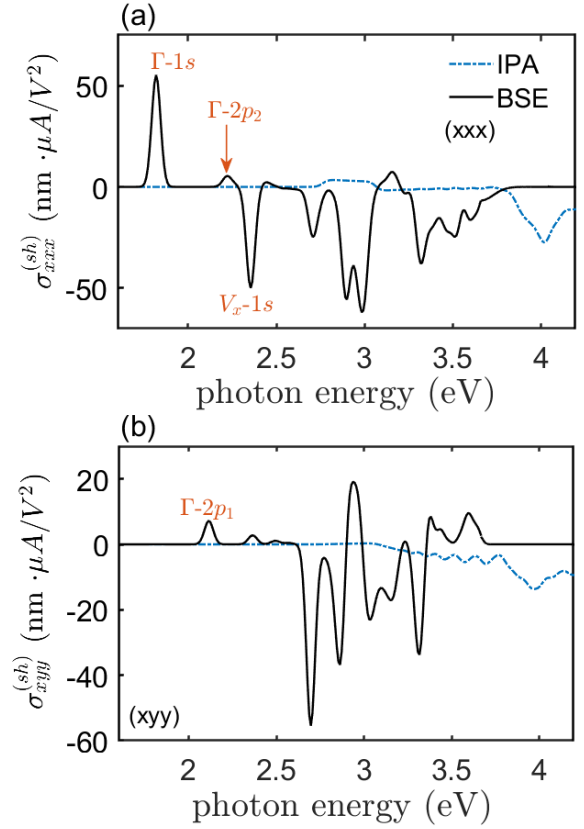


FIG. 4. (a) Component  $xxx$  of the frequency-dependent shift conductivity tensor of monolayer GeS calculated in the IPA approximation and including exciton effects. (b) Same for the  $xyy$  component.

### C. Shift current in short circuit

If light is linearly polarized along the  $x$  direction, the total photogalvanic (shift) current generated in a portion of an hexagonal 2D material with  $D_{3h}$  point group ( $c_2$  rotation axis along  $x$ ) of thickness  $d$  and width  $w$  reads [26, 86]

$$J_x^{(2,DC)}(\omega) = \eta_{\text{inc}}(\omega) \cdot \eta_{\text{abs}}(\omega) \cdot G_{xxx}(\omega) \cdot w \cdot I_x(\omega), \quad (10)$$

where  $\eta_{\text{inc}}(\omega) = 1 - R(\omega)$ ,  $\eta_{\text{abs}}(\omega) = (1 - e^{-\alpha(\omega) \cdot d})$  and  $G_{xxx}(\omega) = 2\sigma_{xxx}^{(sh)}(\omega)[c\epsilon_0\alpha(\omega)]^{-1}$ , known as the *Glass coefficient*.  $R$  and  $\alpha$  stand for reflection and attenuation (or absorption) coefficients, respectively. We omit the Cartesian components of such quantities due to the isotropic in-plane dielectric tensor (in the case of hexagonal 2D materials). It has been argued [86] that the total current is minored if exciton effects are taken into account in calculations, as the magnitude of  $R$  and  $\alpha$  increases, which translates in less current in Eq. (10). However, the change in  $\sigma_{xxx}$  after including exciton effects was not accounted for, which is crucial based on our previous analysis. In monolayer materials,  $\alpha(\omega)^{-1}$  is typically several orders of magnitude smaller than  $d$ . Therefore  $(1 - e^{-\alpha(\omega) \cdot d}) \simeq \alpha(\omega) \cdot d$  and, in the limit of a 2D sample

[87], leads to

$$J_x^{(2,DC)}(\omega) = \frac{\eta_{\text{inc}}(\omega)}{c\epsilon_0} \cdot 2\sigma_{xxx}(\omega) \cdot I_x(\omega) \cdot d \cdot w, \quad (11)$$

which means that the exciton influence is ruled by the changes of the shift conductivity and the reflectivity factor. We assume an intensity of  $1.6 \times 10^4 \text{ W/cm}^2$  and a sample width of  $2 \mu\text{m}$ , as in experiment [25, 26]. We take a monolayer effective thickness for  $\text{MoS}_2$  as reported in Ref. [88], while we use the same value for GeS. In the *Supplementary Material*, we also compare our results for the reflectivity ratio with those obtained after reading the refractive index of Ref. [88], showing a good agreement between the theoretical and experimental excitonic signatures in the spectrum.

In Fig. III C we show the total current generated in a short-circuit configuration with samples of  $\text{MoS}_2$  and GeS. We observe that in-gap  $1s$  excitons give a response of  $\sim 0.5 \cdot 10^{-9} \text{ nA}$  and  $\sim 5 \cdot 10^{-9}$  in  $\text{MoS}_2$  and GeS, respectively; which corresponds to an enlargement by a factor of  $\sim 2$  and  $\sim 9$  with respect to the band-edge response predicted by the IPA calculation of each case. In general, the enhancement due to  $e$ - $h$  interactions in the total current is not as large as in the shift conductivity [see Figs. 1 and 4], due to an additional enhancement of the reflectivity ratio, i.e.,  $\eta_{\text{inc}}(\omega)$  is reduced in Eq. (10) and compensates changes in  $\sigma_{xxx}^{(\text{sh})}$ . Remarkably, the  $2p$  resonances in monolayer  $\text{MoS}_2$  have a similar magnitude than the  $1s$ . This is a consequence of the low oscillator strength of  $2p$  excitons, which gives low reflection at such energies. This feature is not as visible in the  $\Gamma$ - $2p_2$  resonance of GeS, since an optically bright exciton is close in energy and gives a considerable reflectivity. At energies in the continuum, near 3 eV, the response is enlarged to  $\sim 3 \text{ nA}$  in  $\text{MoS}_2$ , while it is inverted in GeS reaching  $\sim -7 \text{ nA}$ , although more bands are needed to fully converge this part of the spectrum.

Photocurrent spectroscopy measurements in monolayer TMDCs allow for the measurement of excitonic resonances with linewidths as low as 8 meV ([89]). Our results show that the  $p$  resonance in the shift photocurrent splits up by 100 meV from the B- $1s$  exciton peak, and gives a comparable current response. It is thus of special importance to take into account the possible impact of this feature when interpreting photogalvanic measurements on TMDC-based experiments.

#### IV. CONCLUSION AND PERSPECTIVE

In this work, we have set up a methodology to calculate excitonic non-linear optical responses based on Wannierized band structures combined with effective electron-hole model interactions. To perform the calculations, we have interfaced the output of the WANNIER90 code with our recently-developed package XATU for solving the BSE. We have developed a post-processing code to

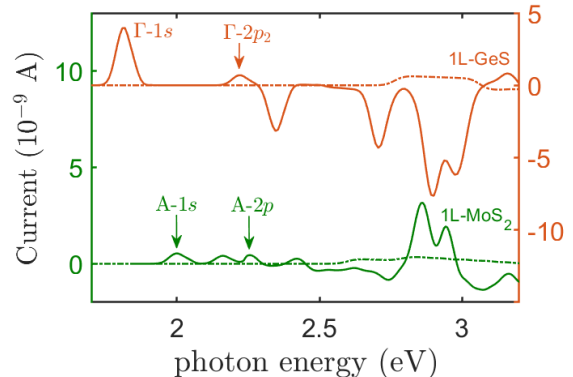


FIG. 5. Total shift current as occurring in a short circuit configuration with 1L- $\text{MoS}_2$  and 1L- $\text{GeS}_2$ , under radiation with monochromatic light. We show the calculation with (solid line) and without (dashed) exciton effects.

calculate the optical response in the linear and second-order regimes. This methodology updates previous works on tight-binding excitons, now by using accurate Wannierization of ab initio band structures. This provides several advantages: multiband effects are captured, the band structure is obtained accurately (including effective masses), and inter-site matrix elements are correctly accounted for. This method thus offers a better description of linear and nonlinear optical responses than empirical tight-binding models.

As examples, we have addressed the role of in-gap excitons in the linear absorbance and shift conductivity of monolayers  $\text{MoS}_2$  and GeS. At low energies, we have shown that the total short circuit current is enlarged by nearly one order of magnitude in GeS due to exciton effects, while this enhancement is lower in  $\text{MoS}_2$ . Remarkably, we have shown that  $2p$  excitons in both cases are clearly visible in the photocurrent spectrum of both materials.

While experimental measurements on  $\text{WS}_2$  do not display any measurable shift-current response, a clear photogalvanic current (under circularly-polarized light) is identified on Ref. [30] in monolayer  $\text{MoSe}_2$ , showing excitonic features. No doubt, more experiments are needed to characterize the exciton fine-structure in the BPVE response in TMDC monolayer samples.

By extending the electron-hole interaction kernel beyond two dimensions, a large variety of systems will be able to be addressed in future works. The post-processing tools used in this work will be available soon in the next version of the XATU code [56], via the package repository.

#### ACKNOWLEDGMENTS

The authors acknowledge financial support from the Spanish MICINN (grants nos. PID2019-109539GB-C43, TED2021-131323B-I00, and PID2022-141712NB-C21),



the María de Maeztu Program for Units of Excellence in R&D (grant no. CEX2018-000805-M), Comunidad Autónoma de Madrid through the Nanomag COST-CM Program (grant no. S2018/NMT-4321), Generalitat Valenciana through Programa Prometeo (2021/017), Centro de Computación Científica of the Universidad Autónoma de Madrid, and Red Española de Supercom-

putación. M.C.-G. is grateful to the Azrieli Foundation for the award of an Azrieli International Postdoctoral Fellowship. Additional computational resources were provided by the Weizmann Institute of Science at Chemfarm. M.C.-G. thanks Tonatiuh Rangel for providing the initial geometries of bulk and monolayer GeS.

---

\* [juan.esteve@uam.es](mailto:juan.esteve@uam.es)

- [1] Nasreen G. Chopra, R. J. Luyken, K. Cherrey, Vincent H. Crespi, Marvin L. Cohen, Steven G. Louie, and A. Zettl. Boron nitride nanotubes. *Science*, 269:966, 1995.
- [2] Feng Wang, Gordana Dukovic, Louis E. Brus, and Tony F. Heinz. The optical resonances in carbon nanotubes arise from excitons. *Science*, 308:838, 2005.
- [3] Kin Fai Mak, Changgu Lee, James Hone, Jie Shan, and Tony F. Heinz. Atomically Thin MoS<sub>2</sub> : A New Direct-Gap Semiconductor. *Physical Review Letters*, 105:136805, 2010.
- [4] Yilei Li, Alexey Chernikov, Xian Zhang, Albert Rigosi, Heather M. Hill, Arend M. van der Zande, Daniel A. Chenet, En-Min Shih, James Hone, and Tony F. Heinz. Measurement of the optical dielectric function of monolayer transition-metal dichalcogenides: MoS<sub>2</sub>, MoSe<sub>2</sub>, WS<sub>2</sub>, and WSe<sub>2</sub>. *Physical Review B*, 90:205422, 2014. Publisher: American Physical Society.
- [5] Ludger Wirtz, Andrea Marini, and Angel Rubio. Excitons in boron nitride nanotubes: Dimensionality effects. *Phys. Rev. Lett.*, 96:126104, 2006.
- [6] Ashwin Ramasubramaniam. Large excitonic effects in monolayers of molybdenum and tungsten dichalcogenides. *Phys. Rev. B*, 86:115409, 2012.
- [7] Diana Y. Qiu, Felipe H. da Jornada, and Steven G. Louie. Optical spectrum of MoS<sub>2</sub>: Many-Body Effects and Diversity of Exciton States. *Physical Review Letters*, 111:216805, 2013. Publisher: American Physical Society.
- [8] Richard M. Martin, Lucia Reining, and David M. Ceperley. *Interacting electrons*. Cambridge University Press, 2016.
- [9] Mads L. Trolle, Gotthard Seifert, and Thomas G. Pedersen. Theory of excitonic second-harmonic generation in monolayer MoS<sub>2</sub>. *Phys. Rev. B*, 89:235410, 2014.
- [10] Emilia Ridolfi, Caio H. Lewenkopf, and Vitor M. Pereira. Excitonic structure of the optical conductivity in MoS<sub>2</sub> monolayers. *Phys. Rev. B*, 97:205409, 2018.
- [11] Maciej Bieniek, Ludmiła Szulakowska, and Paweł Hawrylak. Band nesting and exciton spectrum in monolayer MoS<sub>2</sub>. *Phys. Rev. B*, 101:125423, 2020.
- [12] Diana Y. Qiu, Felipe H. da Jornada, and Steven G. Louie. Screening and many-body effects in two-dimensional crystals: Monolayer MoS<sub>2</sub>. *Phys. Rev. B*, 93:235435, 2016.
- [13] Margherita Marsili, Alejandro Molina-Sánchez, Maurizia Palummo, Davide Sangalli, and Andrea Marini. Spinorial formulation of the GW-BSE equations and spin properties of excitons in two-dimensional transition metal dichalcogenides. *Phys. Rev. B*, 103:155152, 2021.
- [14] Alejandro Molina-Sánchez, Maurizia Palummo, Andrea Marini, and Ludger Wirtz. Temperature-dependent excitonic effects in the optical properties of single-layer MoS<sub>2</sub>. *Phys. Rev. B*, 93:155435, 2016.
- [15] Boris Sturman and Vladimir Fridkin. *Photovoltaic and photo-refractive effects in noncentrosymmetric materials*. Gordon and Breach Science Publishers, 1992.
- [16] Zhenbang Dai and Andrew M. Rappe. Recent progress in the theory of bulk photovoltaic effect. *Chemical Physics Reviews*, 4:011303, 2023.
- [17] W.T.H. Koch, R. Munser, W. Ruppel, and P. Würfel. Bulk photovoltaic effect in BaTiO<sub>3</sub>. *Solid State Communications*, 17:847, 1975.
- [18] W.T.H. Koch, R. Munser, W. Ruppel, and P. Würfel. Anomalous photovoltage in BaTiO<sub>3</sub>. *Ferroelectrics*, 13:305, 1976.
- [19] Ralph von Baltz and Wolfgang Kraut. Theory of the bulk photovoltaic effect in pure crystals. *Physical Review B*, 23:5590, 1981.
- [20] T. Batirov, E. Doubovik, R. Djalalov, and V.M. Fridkin. The bulk photovoltaic effect in the piezoelectric crystal Pr<sub>3</sub>Ga<sub>5</sub>SiO<sub>14</sub>. *Ferroelectrics Letters Section*, 23:95, 1997.
- [21] V. Fridkin, G. Dalba, P. Fornasini, Y. Soldo, F. Rocca, and E. Burattini. The bulk photovoltaic effect in LiNbO<sub>3</sub> crystals under x-ray synchrotron radiation. *Ferroelectrics Letters Section*, 16:1, 1993.
- [22] D. Hornung, R. von Baltz, and U. Rössler. Band structure investigation of the bulk photovoltaic effect in n-gap. *Solid State Communications*, 48:225, 1983.
- [23] K Buse. Light-induced charge transport processes in photorefractive crystals II: Materials. *Applied Physics B*, 64:391, 1997.
- [24] Jonathan E. Spanier, Vladimir M. Fridkin, Andrew M. Rappe, Andrew R. Akbashev, Alessia Polemi, Yubo Qi, Zongquan Gu, Steve M. Young, Christopher J. Hawley, Dominic Imbrenda, et al. Power conversion efficiency exceeding the Shockley-Queisser limit in a ferroelectric insulator. *Nature Photonics*, 10:611, 2016.
- [25] YJ Zhang, Toshiya Ideue, Masaru Onga, Feng Qin, Ryuji Suzuki, Alla Zak, Reshef Tenne, JH Smet, and Yoshihiro Iwasa. Enhanced intrinsic photovoltaic effect in tungsten disulfide nanotubes. *Nature*, 570:349, 2019.
- [26] Jyoti Krishna, Peio Garcia-Goiricelaya, Fernando de Juan, and Julen Ibañez-Azpiroz. Understanding the large shift photocurrent of WS<sub>2</sub> nanotubes: A comparative analysis with monolayers. *Physical Review B*, 108:165418, 2023.
- [27] Guodong Xue, Ziqi Zhou, Quanlin Guo, Yonggang Zuo, Wenya Wei, Jiashu Yang, Peng Yin, Shuai Zhang, Ding Zhong, Yilong You, Xin Sui, Chang Liu, Muhong Wu, Hao Hong, Zhu-Jun Wang, Peng Gao, Qunyang Li, Libo Zhang, Dapeng Yu, Feng Ding, Zhongming Wei, Can Liu, and Kaihui Liu. WS<sub>2</sub> ribbon arrays with defined chirality and coherent polarity. *Science*, 384:1100, 2024.
- [28] Yu Dong, Ming-Min Yang, Mao Yoshii, Satoshi Mat-

- suoka, Sota Kitamura, Tatsuo Hasegawa, Naoki Ogawa, Takahiro Morimoto, Toshiya Ideue, and Yoshihiro Iwasa. Giant bulk piezophotovoltaic effect in 3R-MoS<sub>2</sub>. *Nature nanotechnology*, 18:36, 2023.
- [29] Ruo-Xuan Sun, Zhen Hu, Xuewen Zhao, Ming-Jie Zha, Jinying Zhang, Xu-Dong Chen, Zhibo Liu, and Jianguo Tian. Strain-prompted giant flexo-photovoltaic effect in two-dimensional violet phosphorene nanosheets. *ACS Nano*, 18:13298, 2024.
- [30] Jorge Quereda, Talieh S. Ghiasi, Jhiah-Shih You, Jeroen van den Brink, Bart J. van Wees, and Caspar H. van der Wal. Symmetry regimes for circular photocurrents in monolayer MoSe<sub>2</sub>. *Nature Communications*, 9:3346, 2018.
- [31] Yih-Ren Chang, Ryo Nanae, Satsuki Kitamura, Tomonori Nishimura, Haonan Wang, Yubei Xiang, Keisuke Shinokita, Kazunari Matsuda, Takashi Taniguchi, Kenji Watanabe, et al. Shift current photovoltaics based on a noncentrosymmetric phase in in-plane ferroelectric SnS. *Advanced Materials*, page 2301172, 2023.
- [32] Zihan Liang, Xin Zhou, Le Zhang, Xiang-Long Yu, Yan Lv, Xuefen Song, Yongheng Zhou, Han Wang, Shuo Wang, Taihong Wang, et al. Strong bulk photovoltaic effect in engineered edge-embedded van der Waals structures. *Nature Communications*, 14:4230, 2023.
- [33] Yongheng Zhou, Xin Zhou, Xiang-Long Yu, Zihan Liang, Xiaoxu Zhao, Taihong Wang, Jinshui Miao, and Xiaolong Chen. Giant intrinsic photovoltaic effect in one-dimensional van der Waals grain boundaries. *Nature Communications*, 15:501, 2024.
- [34] M. Sotome, M. Nakamura, J. Fujioka, M. Ogino, Y. Kaneko, T. Morimoto, Y. Zhang, M. Kawasaki, N. Nagaosa, Y. Tokura, and N. Ogawa. Spectral dynamics of shift current in ferroelectric semiconductor SbSI. *Proceedings of the National Academy of Sciences*, 116:1929, 2019.
- [35] M. Sotome, M. Nakamura, T. Morimoto, Y. Zhang, G.-Y. Guo, M. Kawasaki, N. Nagaosa, Y. Tokura, and N. Ogawa. Terahertz emission spectroscopy of ultrafast exciton shift current in the noncentrosymmetric semiconductor CdS. *Phys. Rev. B*, 103:L241111, 2021.
- [36] J. E. Sipe and A. I. Shkrebtii. Second-order optical response in semiconductors. *Phys. Rev. B*, 61:5337, 2000.
- [37] Steve M. Young and Andrew M. Rappe. First principles calculation of the shift current photovoltaic effect in ferroelectrics. *Physical review letters*, 109:116601, 2012.
- [38] Tonatiuh Rangel, Benjamin M. Fregoso, Bernardo S. Mendoza, Takahiro Morimoto, Joel E. Moore, and Jeffrey B. Neaton. Large bulk photovoltaic effect and spontaneous polarization of single-layer monochalcogenides. *Phys. Rev. Lett.*, 119:067402, 2017.
- [39] Ashley M. Cook, Benjamin M. Fregoso, Fernando De Juan, Sinisa Coh, and Joel E. Moore. Design principles for shift current photovoltaics. *Nature communications*, 8(1):14176, 2017.
- [40] Liang Z. Tan, Fan Zheng, Steve M. Young, Fenggong Wang, Shi Liu, and Andrew M. Rappe. Shift current bulk photovoltaic effect in polar materials—hybrid and oxide perovskites and beyond. *Npj Computational Materials*, 2:1, 2016.
- [41] Rui-Chun Xiao, Yang Gao, Hua Jiang, Wei Gan, Changjin Zhang, and Hui Li. Non-synchronous bulk photovoltaic effect in two-dimensional interlayer-sliding ferroelectrics. *npj Computational Materials*, 8:138, 2022.
- [42] Mikkel Ohm Sauer, Alireza Taghizadeh, Urko Petralanda, Martin Ovesen, Kristian Sommer Thygesen, Thomas Olsen, Horia Cornean, and Thomas Garm Pedersen. Shift current photovoltaic efficiency of 2D materials. *npj Computational Materials*, 9:35, 2023.
- [43] Yang Zhang, Tobias Holder, Hiroaki Ishizuka, Fernando de Juan, Naoto Nagaosa, Claudia Felser, and Binghai Yan. Switchable magnetic bulk photovoltaic effect in the two-dimensional magnet CrI<sub>3</sub>. *Nature communications*, 10:3783, 2019.
- [44] Chunmei Zhang, Ping Guo, and Jian Zhou. Tailoring bulk photovoltaic effects in magnetic sliding ferroelectric materials. *Nano Letters*, 22:9297, 2022.
- [45] Swati Chaudhary, Cyprian Lewandowski, and Gil Refael. Shift-current response as a probe of quantum geometry and electron-electron interactions in twisted bilayer graphene. *Phys. Rev. Res.*, 4:013164, 2022.
- [46] Daniel Kaplan, Tobias Holder, and Binghai Yan. Twisted photovoltaics at terahertz frequencies from momentum shift current. *Phys. Rev. Res.*, 4:013209, 2022.
- [47] Z. Ni, K. Wang, Y. Zhang, O. Pozo, B. Xu, X. Han, K. Manna, J. Paglione, C. Felser, Adolfo G. Grushin, et al. Giant topological longitudinal circular photogalvanic effect in the chiral multifold semimetal *cosi*. *Nature communications*, 12:154, 2021.
- [48] Álvaro R. Puente-Uriona, Stepan S. Tsirkin, Ivo Souza, and Julen Ibañez-Azpiroz. Ab initio study of the nonlinear optical properties and dc photocurrent of the Weyl semimetal TaIrTe<sub>4</sub>. *Phys. Rev. B*, 107:205204, 2023.
- [49] Zhenbang Dai and Andrew M. Rappe. First-principles calculation of ballistic current from electron-hole interaction. *Phys. Rev. B*, 104:235203, 2021.
- [50] Yi-Shiuan Huang, Yang-Hao Chan, and Guang-Yu Guo. Large shift currents via in-gap and charge-neutral excitons in a monolayer and nanotubes of BN. *Phys. Rev. B*, 108:075413, 2023.
- [51] Satoru Konabe. Exciton effect on shift current in single-walled boron-nitride nanotubes. *Phys. Rev. B*, 103:075402, 2021.
- [52] Yang-Hao Chan, Diana Y. Qiu, Felipe H. da Jornada, and Steven G. Louie. Giant exciton-enhanced shift currents and direct current conduction with subbandgap photo excitations produced by many-electron interactions. *Proceedings of the National Academy of Sciences*, 118:e1906938118, 2021.
- [53] Chen Hu, Mit H. Naik, Yang-Hao Chan, Jiawei Ruan, and Steven G. Louie. Light-induced shift current vortex crystals in moiré heterobilayers. *Proceedings of the National Academy of Sciences*, 120:e2314775120, 2023.
- [54] Fengcheng Wu, Fanyao Qu, and Allan H MacDonald. Exciton band structure of monolayer MoS<sub>2</sub>. *Physical Review B*, 91:075310, 2015.
- [55] Thomas Galvani, Fulvio Paleari, Henrique P. C. Miranda, Alejandro Molina-Sánchez, Ludger Wirtz, Sylvain Latil, Hakim Amara, and Fran çois Ducastelle. Excitons in boron nitride single layer. *Phys. Rev. B*, 94:125303, 2016.
- [56] Alejandro José Uría-Alvarez, Juan José Esteve-Paredes, Manuel Antonio García-Blázquez, and Juan José Palacios. Efficient computation of optical excitations in two-dimensional materials with the Xatu code, 2023.
- [57] Chong Wang, Xiaoyu Liu, Lei Kang, Bing-Lin Gu, Yong Xu, and Wenhui Duan. First-principles calculation of nonlinear optical responses by Wannier interpolation.

- Phys. Rev. B*, 96:115147, 2017.
- [58] Julen Ibañez-Azpiroz, Stepan S. Tsirkin, and Ivo Souza. Ab initio calculation of the shift photocurrent by Wannier interpolation. *Phys. Rev. B*, 97:245143, 2018.
- [59] Julen Ibañez-Azpiroz, Fernando de Juan, and Ivo Souza. Assessing the role of interatomic position matrix elements in tight-binding calculations of optical properties. *SciPost Phys.*, 12:070, 2022.
- [60] Arash A. Mostofi, Jonathan R. Yates, Young-Su Lee, Ivo Souza, David Vanderbilt, and Nicola Marzari. wannier90: A tool for obtaining maximally-localised Wannier functions. *Computer Physics Communications*, 178:685, 2008.
- [61] Giovanni Pizzi, Valerio Vitale, Ryotaro Arita, Stefan Blügel, Frank Freimuth, Guillaume Géranton, Marco Gibertini, Dominik Gresch, Charles Johnson, Takashi Koretsune, Julen Ibañez-Azpiroz, Hyungjun Lee, Jae-Mo Lihm, Daniel Marchand, Antimo Marrazzo, Yuriy Mokrousov, Jamal I Mustafa, Yoshiro Nohara, Yusuke Nomura, Lorenzo Paulatto, Samuel Poncé, Thomas Ponweiser, Junfeng Qiao, Florian Thöle, Stepan S. Tsirkin, Małgorzata Wierzbowska, Nicola Marzari, David Vanderbilt, Ivo Souza, Arash A. Mostofi, and Jonathan R. Yates. Wannier90 as a community code: new features and applications. *Journal of Physics: Condensed Matter*, 32:165902, 2020.
- [62] David Vanderbilt. *Berry phases in electronic structure theory: electric polarization, orbital magnetization and topological insulators*. Cambridge University Press, 2018.
- [63] Juan José Esteve-Paredes and Juan José Palacios. A comprehensive study of the velocity, momentum and position matrix elements for Bloch states: application to a local orbital basis. *SciPost Phys. Core*, 6:002.1, 2023.
- [64] See discussion around the **WannierTools** package: <https://www.wanniertools.org/theory/tight-binding-model/> (accessed May 2024).
- [65] Michael Rohlfing and Steven G. Louie. Electron-hole excitations and optical spectra from first principles. *Phys. Rev. B*, 62:4927, 2000.
- [66] Diana Qiu, Victor Chang Lee, Marina Filip, Felipe Jornada, and Jack McArthur. Hilbert-space separation schemes in energy-space and real-space for excited-state calculations. In *APS March Meeting Abstracts*, volume 2023, page A59, 2023.
- [67] Maciej Bieniek, Katarzyna Sadecka, Ludmiła Szulakowska, and Paweł Hawrylak. Theory of excitons in atomically thin semiconductors: tight-binding approach. *Nanomaterials*, 12:1582, 2022.
- [68] Pierluigi Cudazzo, Ilya V. Tokatly, and Angel Rubio. Dielectric screening in two-dimensional insulators: Implications for excitonic and impurity states in graphene. *Phys. Rev. B*, 84:085406, 2011.
- [69] Alexandre C. Dias, Julian F.R.V. Silveira, and Fanyao Qu. WanTiBEXOS: A Wannier based Tight Binding code for electronic band structure, excitonic and optoelectronic properties of solids. *Computer Physics Communications*, 285:108636, 2023.
- [70] Høgni C. Kamban and Thomas G. Pedersen. Interlayer excitons in van der Waals heterostructures: Binding energy, Stark shift, and field-induced dissociation. *Scientific reports*, 10:5537, 2020.
- [71] Cesar E. P. Villegas and Alexandre R. Rocha. Screened hydrogen model of excitons in semiconducting nanoribbons. *Phys. Rev. B*, 109:165425, 2024.
- [72] Junyeong Ahn, Guang-Yu Guo, and Naoto Nagaosa. Low-frequency divergence and quantum geometry of the bulk photovoltaic effect in topological semimetals. *Phys. Rev. X*, 10:041041, 2020.
- [73] Manuel Antonio García-Blázquez, Juan José Esteve-Paredes, Alejandro José Uría-Álvarez, and Juan José Palacios. Shift current with gaussian basis sets and general prescription for maximally symmetric summations in the irreducible Brillouin zone. *Journal of Chemical Theory and Computation*, 19:9416, 2023.
- [74] Alireza Taghizadeh, F. Hipolito, and T. G. Pedersen. Linear and nonlinear optical response of crystals using length and velocity gauges: Effect of basis truncation. *Phys. Rev. B*, 96:195413, 2017.
- [75] Thomas Garm Pedersen. Intraband effects in excitonic second-harmonic generation. *Phys. Rev. B*, 92:235432, 2015.
- [76] Alireza Taghizadeh and T. G. Pedersen. Gauge invariance of excitonic linear and nonlinear optical response. *Phys. Rev. B*, 97:205432, 2018.
- [77] Ashwin Ramasubramaniam, Dahvyd Wing, and Leeor Kronik. Transferable screened range-separated hybrids for layered materials: The cases of MoS<sub>2</sub> and h-BN. *Phys. Rev. Mater.*, 3:084007, 2019.
- [78] María Camarasa-Gómez, Ashwin Ramasubramaniam, Jeffrey B. Neaton, and Leeor Kronik. Transferable screened range-separated hybrid functionals for electronic and optical properties of van der Waals materials. *Phys. Rev. Mater.*, 7:104001, 2023.
- [79] Timothy C. Berkelbach, Mark S. Hybertsen, and David R. Reichman. Theory of neutral and charged excitons in monolayer transition metal dichalcogenides. *Phys. Rev. B*, 88:045318, 2013.
- [80] Diana Y. Qiu, Ting Cao, and Steven G. Louie. Non-analyticity, valley quantum phases, and lightlike exciton dispersion in monolayer transition metal dichalcogenides: Theory and first-principles calculations. *Phys. Rev. Lett.*, 115:176801, 2015.
- [81] Fang Zhang, Chin Shen Ong, Jia Wei Ruan, Meng Wu, Xing Qiang Shi, Zi Kang Tang, and Steven G. Louie. Intervalley excitonic hybridization, optical selection rules, and imperfect circular dichroism in monolayer h-BN. *Phys. Rev. Lett.*, 128:047402, 2022.
- [82] M. F. C. Martins Quintela and T. Garm Pedersen. Anisotropic linear and nonlinear excitonic optical properties of buckled monolayer semiconductors. *Phys. Rev. B*, 107:235416, 2023.
- [83] Alireza Taghizadeh and T. G. Pedersen. Nonlinear optical selection rules of excitons in monolayer transition metal dichalcogenides. *Phys. Rev. B*, 99:235433, 2019.
- [84] Jiawei Ruan, Y. H. Chan, and Steven G. Louie. Excitonic effects in nonlinear optical responses: Exciton-state formalism and first-principles calculations, 2023.
- [85] Lidia C. Gomes, P. E. Trevisanutto, A. Carvalho, A. S. Rodin, and A. H. Castro Neto. Strongly bound mott-wannier excitons in GeS and GeSe monolayers. *Phys. Rev. B*, 94:155428, 2016.
- [86] Ruixiang Fei, Liang Z. Tan, and Andrew M. Rappe. Shift-current bulk photovoltaic effect influenced by quasiparticle and exciton. *Phys. Rev. B*, 101:045104, 2020.
- [87] We numerically check that Eqs. (10) and (11) give nearly identical curves (not shown).
- [88] Hsiang-Lin Liu, Teng Yang, Jyun-Han Chen, Hsiao-Wen

- Chen, Huaihong Guo, Riichiro Saito, Ming-Yang Li, and Lain-Jong Li. Temperature-dependent optical constants of monolayer MoS<sub>2</sub>, MoSe<sub>2</sub>, WS<sub>2</sub>, and WSe<sub>2</sub>: spectroscopic ellipsometry and first-principles calculations. *Scientific reports*, 10:15282, 2020.
- [89] Daniel Vaquero, Vito Clericò, Juan Salvador-Sánchez, Adrián Martín-Ramos, Elena Díaz, Francisco Domínguez-Adame, Yahya M. Meziani, Enrique Diez, and Jorge Quereda. Excitons, trions and rydberg states in monolayer MoS<sub>2</sub> revealed by low-temperature photocurrent spectroscopy. *Communications Physics*, 3:194, 2020.